

On-Orbit Performance & Operation of the Attitude & Pointing Control Subsystems on ASTERIA

Christopher M. Pong
 Jet Propulsion Laboratory, California Institute of Technology
 4800 Oak Grove Drive, Pasadena, CA 91109; 818-354-5992
 Christopher.M.Pong@jpl.nasa.gov

ABSTRACT

The Arcsecond Space Telescope Enabling Research in Astrophysics (ASTERIA) is a 6U CubeSat that was deployed from the International Space Station on 20 November 2017. The underlying goal of the mission is to image and perform photometry on bright, nearby stars and possibly detect transiting exoplanets orbiting these stars. As a technology demonstration with an eye to enable this science, the payload must be pointed with a stability of 5 arcseconds RMS over 20-minute observations and a repeatability of 1 arcsecond RMS across multiple observations. A two-stage control system was employed to achieve these pointing requirements: reaction wheels control the attitude of the spacecraft bus while a piezo stage translates the focal plane array to control the pointing of the payload. This paper will present on-orbit results that demonstrate a pointing stability of 0.5 arcsecond RMS over 20 minutes and a pointing repeatability of 1 milliarcsecond RMS from observation to observation, the best pointing of a CubeSat to date. In addition, this paper will discuss the pointing achieved by the attitude control subsystem alone, pointing issues due to temporarily bright pixels, hot pixels, and reaction wheel speed reversals or zero crossings, the deployment and Sun acquisition phase, momentum management issues arising from a large residual dipole, and some of the anomalies encountered with the attitude control subsystem.

BACKGROUND

The Arcsecond Space Telescope Enabling Research in Astrophysics (ASTERIA) was the first CubeSat designed and integrated by the Jet Propulsion Laboratory (JPL) to have been successfully operated in space. Table 1 shows a timeline of the major events from the project kickoff to the deployment from the International Space Station (ISS) at an altitude of 400 kilometers and inclination of 51.6 degrees.

Table 1: ASTERIA Project Timeline.

Date	Event
2014 October 24	Project Kickoff
2015 March 3	Mission Concept Review System Requirements Review
2016 February 24-25	Design Review
2017 June 1	Delivery to NanoRacks
2017 August 14	Launch to ISS on SpaceX CRS-12
2017 November 20	Deployment from ISS

The project had a fairly aggressive, three-year schedule, which is very fast for a JPL flight project. As such, relatively little has been published on ASTERIA to date, which will change in the near future. However, ASTERIA actually traces its roots back to the ExoplanetSat project, led by the Massachusetts Institute of Technology.¹⁻⁸ The purpose of the ExoplanetSat

project was to discover transiting exoplanets around the nearest, brightest, Sun-like stars. While the underlying goal of ASTERIA is still the same, the main mission requirements are actually to demonstrate key technologies for enabling photometry on small satellites. The two main pointing requirements are to demonstrate 5 arcsecond RMS pointing stability over 20-minute observations and 1 arcsecond RMS pointing repeatability from observation to observation. The pointing should remain stable over an observation due to the intra-pixel gain variations and the pointing should be repeatable between observations due to the inter-pixel gain variations. If the light from a star hits different parts of a pixel, that can cause a change in measured flux of the star. This effect can be reduced by increasing the size of the point spread function (PSF) relative to the size of a pixel, but this must be balanced against the increase in other noise sources such as read noise and dark current. Pointing error plays an important role in the overall photometric noise budget.

To put ASTERIA in context with other space missions, Figure 1 shows a plot of the RMS pointing stability (and the time period over which the stability applies) versus mass for various missions. This plot includes the Hubble Space Telescope (HST),⁹ James Webb Space Telescope (JWST),¹⁰ Chandra X-Ray Observatory (CXO),¹¹ Solar Dynamics Observatory (SDO),¹² Infrared Space Observatory (ISO),¹¹ Planetary Transits

and Oscillations of Stars (PLATO),¹³ Kepler,¹⁴ AKARI,¹¹ Spitzer Space Telescope (SST),¹⁵ Wide-Field Infrared Survey Explorer (WISE),¹¹ Convection Rotation and Planetary Transits (CoRoT),¹⁶ Transiting Exoplanet Survey Satellite (TESS),¹⁷ Galaxy Evolution Explorer (GALEX),¹¹ Characterising Exoplanets Satellite (CHEOPS),¹⁸ Microvariability and Oscillations of Stars Telescope (MOST),¹⁹ Bright-Star Target Explorer (BRITE),²⁰ Miniature X-ray Solar Spectrometer (MinXSS),²¹ and Optical Communication and Sensor Demonstration (AeroCube-OCSD-B/C).²² This is by no means a complete list of all missions. If a mission was left out, it was either because complete, publicly available information about the pointing capability could not be found or the author was unaware of the mission at the time of writing. The plot makes a distinction between missions that have not launched versus missions that have launched. It also denotes pointing stability numbers that are requirements versus estimated performance. As can be seen, ASTERIA has the best pointing stability performance to date for spacecraft of its size and is on par with other spacecraft that are orders of magnitude larger.

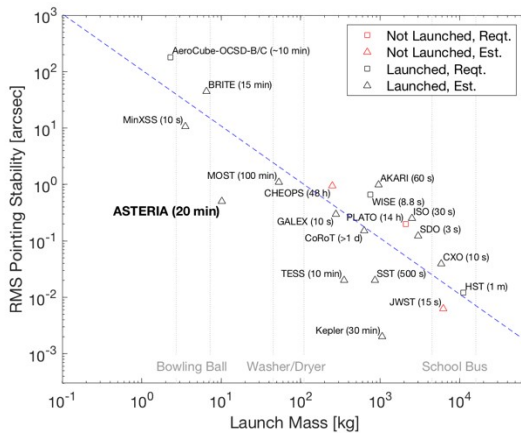


Figure 1: Pointing Stability vs. Mass of Various Missions.

This paper will first discuss the hardware and software design of the attitude and pointing control subsystems, then present their operation and performance on orbit, including (1) the pointing performance of the payload for various observations, including pointing performance achieved by the attitude control system alone, (2) pointing issues & the associated workarounds, (3) the deployment & sun acquisition phase, (4) momentum management issues due to a large spacecraft residual dipole, and (5) anomalies with the attitude control subsystem.

HARDWARE & SOFTWARE DESIGN

This section will provide a brief overview of the spacecraft, followed by a high-level overview of the attitude and pointing control hardware and software design.

Spacecraft

Figure 2 shows a picture of the final spacecraft prior to delivery with the solar arrays deployed. Various parts are highlighted, including the payload, star tracker, sun sensor, GPS antenna, and S-band antenna. In the picture, the spacecraft is propped up on handles, which are only for handling on the ground and are not a part of the spacecraft. The picture also shows the direction of the spacecraft-fixed x -, y -, and z -axes. The x -axis is aligned with the nominal payload boresight, the z -axis is antiparallel with the nominal solar panel normal vector and sun sensor boresight, and the y -axis completes a dextral triad.

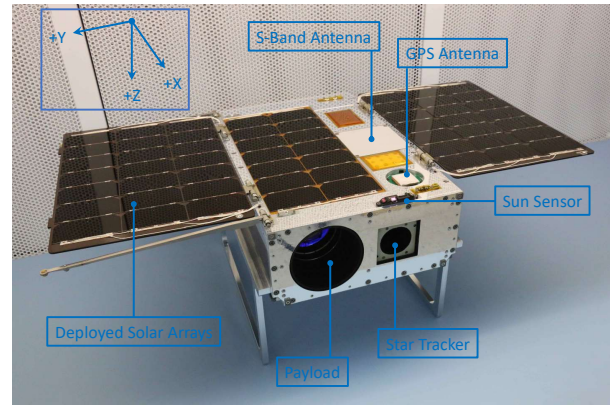


Figure 2: ASTERIA with Deployed Solar Arrays.

The mass, dimensions, center of mass, and moments of inertia are shown in Table 2. The mass, center of mass, and moments of inertia were all measured at the Environmental Test Laboratory at JPL with the completed spacecraft. The center of mass lists two values since two separate measurements were made in two different orientations. As mentioned in the Momentum Management & Residual Dipole section on page 15, the center of mass is important to ensure aerodynamic drag is small enough to be able to control the momentum of the spacecraft. The measured center of mass meets requirements and was able to be achieved without the use of trim masses. The spacecraft was designed to ensure mass was roughly equally distributed in the x - y plane of the spacecraft.

Table 2: ASTERIA Mass Properties.

Variable	Value
Mass (measured)	10.165 kg
Dimensions between largest flat surfaces of chassis (designed)	366 mm (x-axis) 239.4 mm (y-axis) 106.2 mm (z-axis)
Center of mass relative to geometric center with solar arrays deployed (measured)	-2.07 to -1.78 mm (x-axis) -5.52 to -4.67 mm (y-axis) -1.37 to -1.35 mm (z-axis)
Moments of inertia about center of mass with solar arrays deployed (measured)	0.0969 kgm ² (x-axis) 0.1235 kgm ² (y-axis) 0.1918 kgm ² (z-axis)

Further information about the spacecraft and its various subsystems can be found in Ref. 23.

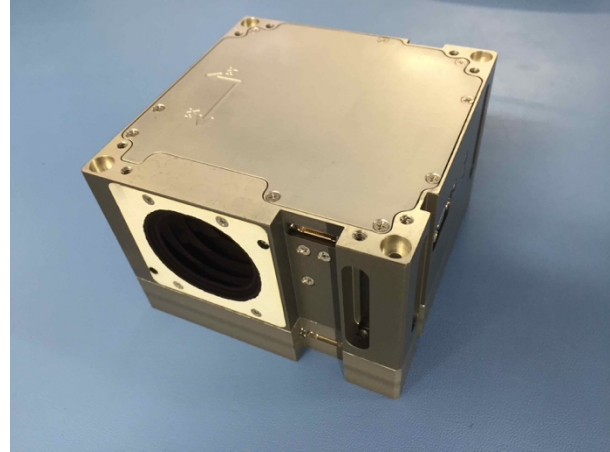
Attitude Control Subsystem Hardware & Software

The attitude control subsystem (ACS) used on ASTERIA is the Blue Canyon Technologies (BCT) fleXible Attitude Control Technology (XACT), shown in Figure 3. This is a fully integrated subsystem with both hardware and software necessary to control the spacecraft's attitude.

The sensors include a star tracker, inertial measurement unit (IMU), sun sensor, and magnetometer. The sun sensor, consisting of four diodes, is mounted on the $-z$ -face of the spacecraft and is aligned with the nominal solar array normal vector. This allows the XACT to point the solar arrays to the Sun but does not provide full-sky coverage.

The actuators include three reaction wheels for attitude control and three torque rods for momentum control.

A GPS unit was also added to the unit to assist with providing accurate time, position, and velocity information to the XACT and spacecraft. Unfortunately, due to issues with the flight harness (not the XACT or GPS unit itself), the GPS could not be powered on properly during testing close to delivery of the spacecraft. Therefore, the GPS was not attempted to be powered on in space thus far. This has little impact on the performance of the XACT or spacecraft but does result in additional operational overhead by needing to supply time, position, and velocity information to the XACT via ground command.

**Figure 3: ASTERIA's Flight XACT Unit.**

The software on the XACT includes algorithms for star tracking, attitude estimation, attitude control, momentum control, and orbit propagation. The primary commands used by ASTERIA to control the XACT include: setting the time, setting the position and velocity, pointing to the Sun, pointing to an inertial attitude, pointing to a specified target, setting the momentum bias (specifically requested for ASTERIA and is now a part of the standard XACT commands), and setting the attitude control gains. The software and hardware on the XACT provided turnkey ACS capability for ASTERIA.

Pointing Control Subsystem Hardware

During science observations, while the ACS provides attitude control with reaction wheels, the pointing of the payload is further improved with the pointing control subsystem (PCS). This consists of three main pieces of hardware: a lens assembly, a piezo stage, and an imager, which are all components of the payload.

The lens assembly, shown in Figure 4, was nominally designed to have a focal length of 85 millimeters and an f-number of 1.4. The lenses, lens rings, lens housing, bipods, baffle, mounting plates, and enclosure were all designed and integrated at JPL.

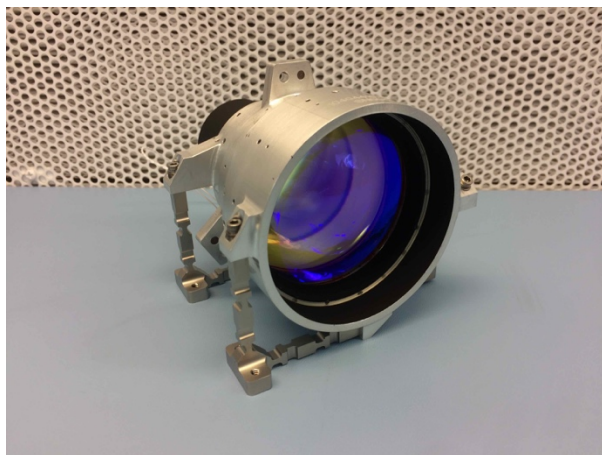


Figure 4: ASTERIA's Flight Lens Assembly.

The two-axis piezoelectric nanopositioning stage, shown in Figure 5, is a Physik Instrumente P-733K110, which is a customized version of the off-the-shelf P-733.2CD. This stage is mounted behind the lens assembly and provides the ability to translate the imager in the plane orthogonal to the payload boresight, effectively providing a tip/tilt correction used to stabilize the image of the star field being observed. This piezo stage has a stroke of ± 50 micrometers in each axis and has two strain gauges to measure the position of each axis. The electronics to control the piezo stage were designed and integrated at JPL. It contains a digital-to-analog converter to command the stage, an analog-to-digital converter to read the position of the stage, two high-voltage amplifiers to drive each axis, a strain gauge feedback loop to remove hysteresis, and a notch filter to avoid exciting the resonant frequency of the moving mass of the stage.

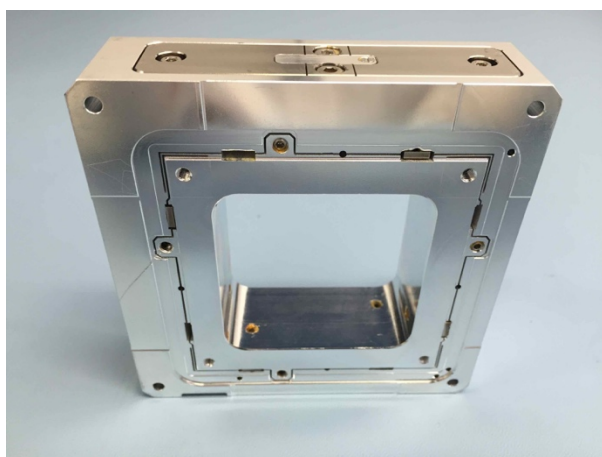


Figure 5: ASTERIA's Flight Piezo Stage.

Mounted to this piezo stage is a Fairchild Imaging CIS2521F0111. This is a frontside-illuminated, monochrome CMOS image sensor with 2592 by 2192

pixels and a 6.5-micrometer pixel pitch. With the lens, the imager has a field of view of 11.2 by 9.6 degrees and each pixel is 15.8 arcseconds on a side. The electronics and harnessing to drive the imager were designed and integrated by Ecliptic Enterprises Corporation. The firmware to control the imager was developed by JPL.

Pointing Control Subsystem Software

The software that performs the fine pointing control is depicted in the block diagram shown in Figure 6. The software is made up of four algorithms: centroiding, target star centering, pointing control, and piezo & roll offload. These algorithms all run at 20 Hz.

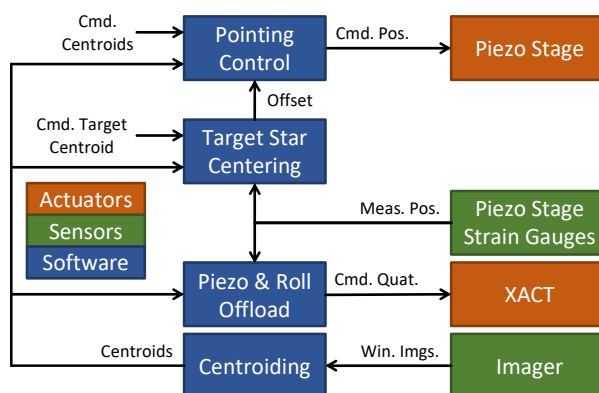


Figure 6: Block Diagram of Pointing Control Software.

The centroiding algorithm receives up to eight 64-by-64-pixel windows from the imager, calculates the centroid of the star in each of these windows, and reports the validity of these centroids. The first step is to correct the images for artifacts and the background flux. Each column in the detector has a bias that is constant over time and independent of integration time, which is referred to as the column offset. The images are corrected by subtracting these column offsets and then subtracting the average background of each window, while ensuring the value of a pixel remains nonnegative. Then, the centroids are computed by searching an area of each window for the brightest pixel, creating a region of interest (ROI) around this brightest pixel, and computing the center of mass of the corrected image in this ROI. As will be discussed in the Pointing Issues & Workarounds section on page 12, the centroiding algorithm actually needed to be modified slightly to be more robust to temporarily bright or hot pixels.

These centroids are then fed into the three other pointing control algorithms, the first of which is the target star centering algorithm. The purpose of this algorithm is to compute an offset that, when used by the

pointing control algorithm, centers the target star. The target star is simply a special guide star that is chosen to have zero control error bias. Since there are up to eight guide stars and all the measured centroids cannot necessarily be driven to their commanded locations with zero error due to effects such as PSF shape or star catalog errors, each guide star can have some residual error. However, one of these stars, the target star, is selected to be driven to its commanded location with zero bias. The error between the commanded and measured target star centroid is integrated and multiplied by a gain to form the target star offset. To avoid integrator windup, this integration is only performed if the piezo stage is not close to saturation.

This target star offset, along with the measured centroids of all the guide stars are fed into the pointing control algorithm. This algorithm first computes the weighted average of the error of the guide stars. The weights are computed as the inverse of the variance of each centroid measurement, which are based on a priori estimates from imager and centroiding simulations. Since variance increases as stars get dimmer, this effectively puts more weight on brighter stars and less weight on dimmer stars. This combined guide star error is summed with the target star offset, forming the control error. Note that this combination of the target and guide stars is effectively a complementary filter. At low frequencies, the error is computed from the target star alone, allowing the target star to be controlled to have zero bias. At high frequencies, the control error is computed from the combination of all the guide stars to reduce the high-frequency noise in the control error. The crossover frequency of this complementary filter is determined by the gain in the target star centering algorithm. The control error is then saturated to avoid overshoot and fed through an 8th-order discrete-time transfer function to compute the commanded piezo stage position. To avoid controller windup, if the commanded position is beyond the saturation limits, the command is saturated and the control history in the discrete transfer function state is also modified to reflect this saturation. This command is then sent to the piezo stage to stabilize the image.

Finally, the piezo stage and roll offload algorithm is used to command the ACS to roughly center the piezo stage, keeping it away from the saturation limits, as well as roughly zero the roll-about-boresight angle observed by the payload. This is done by constructing an attitude quaternion command based on a tip and tilt command offset and a roll command offset. The tip and tilt command offsets are computed by taking the error between the measured and centered piezo stage position, integrating it, and multiplying it by a gain. The roll command is computed from the roll error, which

can be computed from the relative motion of the guide stars spread across the imager. Roughly speaking, if a star near the top of the imager moves left while a star near the bottom of the imager moves right, it can be determined how much the spacecraft must have rolled to produce that centroid motion. This roll error is integrated and multiplied by a gain to produce the roll command. The tip, tilt, and roll commands are used to construct a delta quaternion that is multiplied with the nominal quaternion command and sent to the XACT. The gains used for computing the tip, tilt, and roll commands determine how quickly the piezo stage and roll error are offloaded to the attitude controller. While the commanded quaternion is computed at 20 Hz, the commands to the XACT are downsampled to 5 Hz.

With this description of the design of the attitude and pointing control subsystems, their operation and performance on orbit can now be presented.

ON-ORBIT OPERATION & PERFORMANCE

This section is split into five main topics covering the on-orbit ACS and PCS operation and performance: (1) pointing performance, (2) pointing issues & workarounds (3) deployment & sun acquisition, (4) momentum management & residual dipole, and (5) XACT anomalies.

Pointing Performance During Science Observations

ASTERIA has performed many successful observations of various star fields. To serve as an example of the pointing performance that was achieved with the XACT and PCS operating together, observations of HD 219134, 55 Cancri, and Alpha Centauri will be presented. In addition, pointing performance from the XACT alone, as measured by the payload, will also be presented.

Payload Pointing Performance (HD 219134)

The first star field that was observed was around HD 219134. At this point it is worth describing how the guide star catalog is generated and how guide stars are selected and placed for an observation. Starting with the Hipparcos star catalog,²⁴ stars that have neighbors within a certain angular distance (within a few pixels) were merged into a single star with a new, combined direction and magnitude, as these stars cannot be distinguished as separate stars. Then, stars with neighbors within a certain magnitude range (V magnitude of 2.5) and angular range (the diagonal size of the window) were removed from the catalog, as their close proximity with each other would interfere with the centroiding algorithm. For an observation, the target star is chosen along with a desired pixel location on the detector and roll angle. This defines the attitude that

must be achieved for this observation geometry. The remaining guide stars are then chosen as the brightest stars within the field of view of the imager. If any star is in an undesirable location (e.g., hot pixel near the star), the target star location and/or roll angle can be adjusted to move all of the guide star windows around.

The star field around HD 219134 (HIP 114622) can be seen in Figure 7. This plot shows stars down to a V magnitude of 9 within the circular field of view of the lens. Within this area, it shows the rectangular field of view of the imager and the guide stars that were selected. Each guide star is labeled with the star index (1 through 8) and the Hipparcos catalog identifier. Star 1 is the target star and stars 2 through 8 are the other guide stars. The selected guide stars have a V magnitude in the range of 4.9 to 5.7.

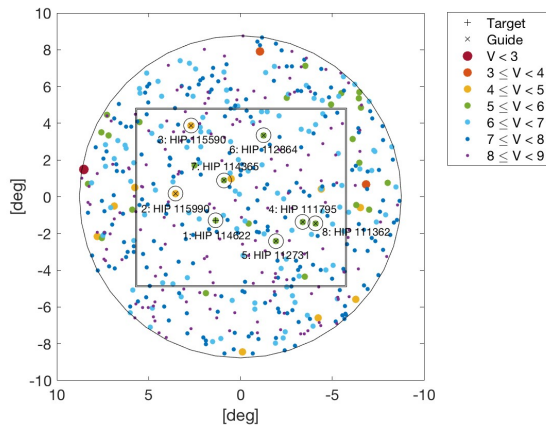


Figure 7: Selected Target & Guide Stars for HD 219134 Observation.

For this particular observation, example images of the eight guide stars can be seen in Figure 8. These are 64-by-64-pixel, windowed images with integration times of 50 milliseconds, coadded over a minute. Also, there are significant column offsets, which are removed for each window by subtracting the median value of each column from each pixel. The point spread functions are spread over many pixels, which was done intentionally for centroiding and photometry purposes. Note that each window has only one clearly visible star due to the care taken when generating the guide star catalog.

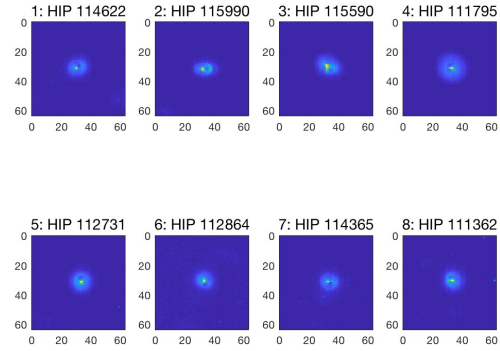


Figure 8: Windowed Images of Target and Guide Stars for HD 219134 Observation.

Before describing the results, it is important to describe how the cross-boresight pointing and attitude errors are calculated. The pointing error is computed from the target and guide stars imaged by the payload. This is actually equivalent to the control error discussed in the Pointing Control Subsystem Software section on page 4. The attitude error is computed by combining the pointing error with the piezo stage position to determine the pointing error that would have resulted, if the piezo stage were not moving. It is important to note that the attitude error reported for the standard observations are not representative of how the XACT would perform alone for two reasons. First, the attitude controller is detuned to improve pointing performance. This will be discussed further later in this section. Second, the payload is feeding quaternion commands to the XACT, which affect the attitude errors. For the payload pointing performance with the XACT alone, see the XACT-Only Pointing Performance (Alpha Centauri) section on page 10.

The cross-boresight attitude and pointing errors for one 20-minute observation of HD 219134 can be seen in Figure 9. This can be thought of as the path of the target star on the imager over time, without and with the piezo stage active. Note that the x - and y -axes refer to the payload imager reference frame and not the spacecraft reference frame shown in Figure 2. The bias and standard deviation for each axis of the attitude and pointing errors are shown in the legend. This performance is consistent across many observations. This specific star field with the same star placement was observed over 50 times in a span of three months. Due to limited communication bandwidth and ground station passes, pointing data for only 9 of these observations were downlinked. For these 9 observations, the pointing repeatability was 1 milliarcsecond RMS and the pointing stability was 0.5

arcsec RMS over 20 minutes. This pointing stability corresponds to approximately $1/30^{\text{th}}$ of a pixel. This is the best pointing stability achieved to date on a spacecraft of this size (see Figure 1).

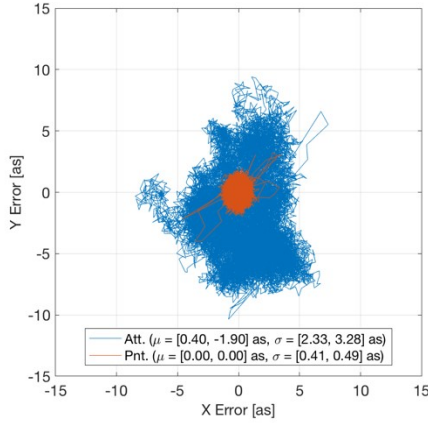


Figure 9: Attitude & Pointing Error Scatter Plot for HD 219134 Observation.

To get a better sense of the nature of these errors, the attitude and pointing errors are plotted versus time in Figure 10. This shows that the attitude error contains a significant low-frequency wandering. This is largely due to the environmental torques acting on the spacecraft and the fact that the attitude controller bandwidth was purposefully detuned to 0.03 Hz. While detuning the attitude controller bandwidth results in larger attitude errors, it pushes more error into lower frequencies, allowing the pointing controller to remove more error overall. This detuning was balanced against the limited stroke of the piezo stage. In fact, an attitude controller bandwidth of 0.02 Hz was used on-orbit for a few observations until it resulted in a few instances of the piezo stage saturating. So, a bandwidth of 0.03 Hz was settled upon for all subsequent observations. This detuning strategy was shown to improve the on-orbit pointing performance by 20%.

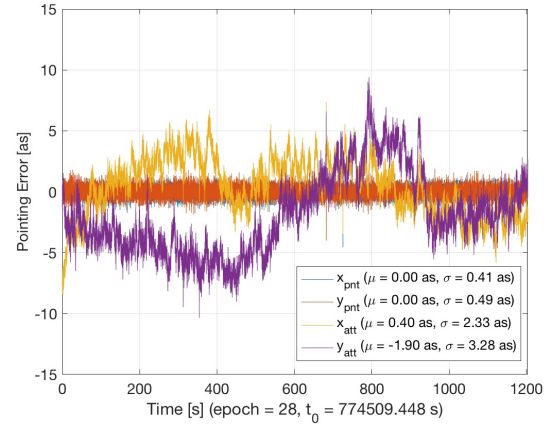


Figure 10: Attitude & Pointing Error vs. Time for HD 219134 Observation.

The power spectral density (PSD) and cumulative mean square value (MSV), integrated in both directions, of the attitude and pointing errors are shown in Figure 11. This plot reveals several key pieces of information about the system.

First, the highest frequency in the plot is 10 Hz, which is the Nyquist frequency, given the pointing control sampling rate of 20 Hz. This means that any errors higher than 10 Hz are not captured in this measured data. Also, it is unlikely that higher frequency errors would be aliased down into the lower frequency range due to the effective low-pass filtering of the imager due to the 50-ms integration time. In other words, high-frequency errors, such as reaction wheel jitter, would manifest as smearing of the stellar images, but would not be seen in the measured error. Further discussion of the effect of reaction wheel jitter on the pointing error for ASTERIA can be found in Ref. 25. The effect of reaction wheel jitter was expected to be a minor contribution to the overall pointing error.

Second, the plot of the PSD flattens out in the range of 4 to 10 Hz. This is the noise floor of the centroids, which is measurement error that should not be included when computing the true pointing error. Nevertheless, this error is kept in since, as mentioned in the previous paragraph, there are errors above 10 Hz that may be present but are not seen in the measured data.

Third, the attitude and pointing PSDs and cumulative MSVs diverge at 2 Hz, which is the bandwidth of the pointing controller. Above 2 Hz, the attitude and pointing PSDs and MSVs lie on top of each other. However, below 2 Hz, the pointing controller removes a significant portion of the attitude error.

Finally, the last feature of the plot is that the pointing error cumulative MSV flattens out at low frequencies. This means that the pointing stability, while measured over 20 minutes, would likely not change for longer observation times. The pointing control algorithms were designed for this to be the case.

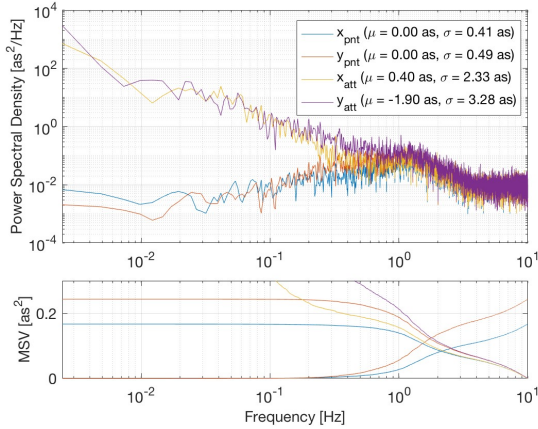


Figure 11: Attitude & Pointing Error Power Spectral Density and Mean Square Value for HD 219134 Observation.

In addition to the cross-boresight pointing errors, there is also the pointing error associated with a roll about the payload boresight. This roll error does not matter as much as the cross-boresight pointing errors since it takes a relatively large amount of angular error to result in a significant amount of motion of the guide stars. It also means that measurements of roll will be noisier than measurements of the cross-boresight pointing errors.

The computed roll error and roll command can be seen in Figure 12. The mean and standard deviation of the roll error are in the legend. Recall that the piezo stage only controls two translational degrees of freedom, so the roll axis is controlled just by the reaction wheels. To ensure the roll error has roughly zero bias, the roll error is used to compute a roll command, which is the roll component of a quaternion command that is fed back to the attitude controller. It can be seen that the roll command drifted by up to 60 arcseconds, while the roll error bias stayed near zero over the 20-minute observation. The 60-arcsecond change in roll command over the observation is attributed to changes in the alignment of the star tracker versus the payload from thermomechanical distortion of various structural elements. This alignment change is within expectations given that the temperature of the bus changes by roughly 15 degrees Kelvin between orbit day and night.

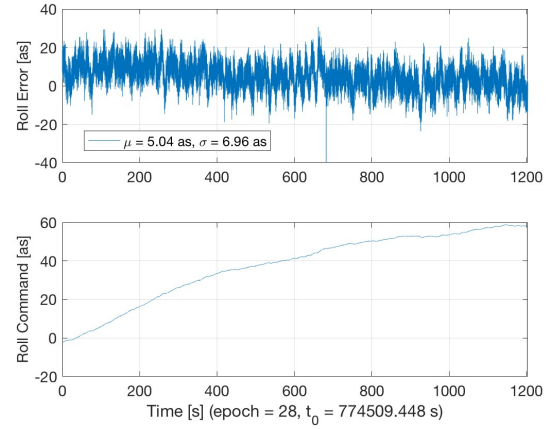


Figure 12: Roll Error & Resulting Command vs. Time for HD 219134 Observation.

In addition to the roll component, the commanded quaternion sent to the attitude controller is composed of a tip and tilt component. The tip and tilt components are used to keep the piezo stage roughly centered and far from the saturation limits. This is computed from the piezo stage error, the difference between the measured piezo stage position and a centered piezo position. These quantities are plotted in Figure 13. This shows that the piezo stage is kept roughly centered (well within the $\pm 50 \mu\text{m}$ range) and the cross-boresight alignment between the star tracker and payload has an initial bias of 10-40 arcseconds and drifts by up to 30 arcseconds over this observation. Without the piezo stage offload, the piezo stage would have had a bias up of to 35% of its range, increasing the chance that it could have been saturated.

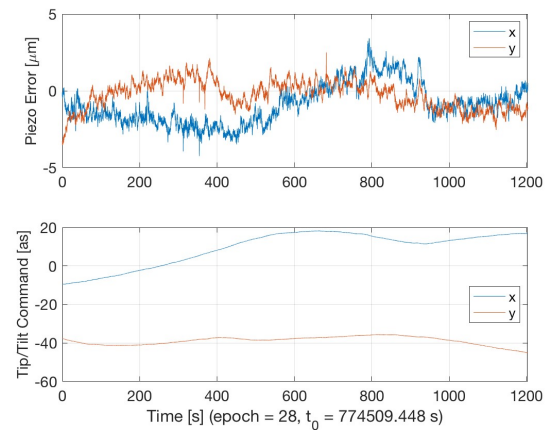


Figure 13: Piezo Stage Error & Resulting Command vs. Time for HD 219134 Observation.

Payload Pointing Performance (55 Cancri)

Since the number and brightness of the target and guide stars has a large effect on the pointing performance, an example of the pointing performance for another star field, 55 Cancri, is presented. Figure 14 shows the selected target and guide stars for this observation. There are seven target and guide stars with V magnitudes in the range of 5.2 to 6.0. The eighth star is not used for control and is actually 55 Cancri (HIP 43587). This is because 55 Cancri has a neighboring star, 53 Cancri, that would interfere with the centroiding algorithm (see Figure 15). The guide star closest to 55 Cancri was selected as the target star.

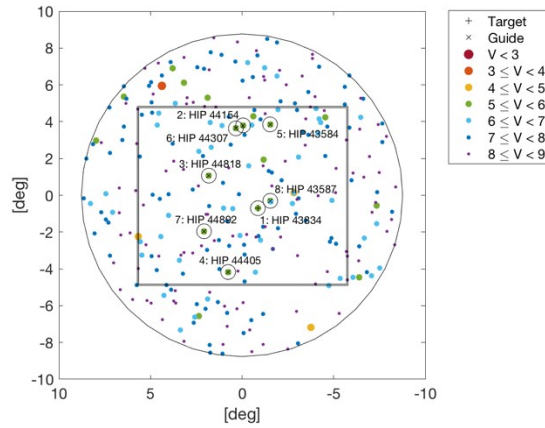


Figure 14: Selected Target and Guide Stars for 55 Cancri Observation.

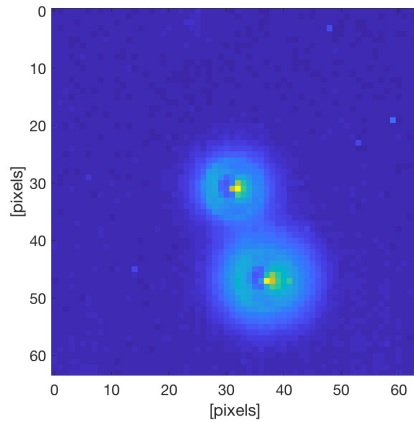


Figure 15: Image of 55 Cancri (Center) and 53 Cancri (Bottom Right).

Since the target and guide stars selected are dimmer than those selected for the HD 219134 observation, it is expected that the pointing performance will be slightly worse due to larger noise in the centroid measurements of these stars. The attitude and pointing error can be seen in Figure 16, which indeed show slightly worse

performance with a pointing stability of 0.7 arcsec RMS over 20 minutes.

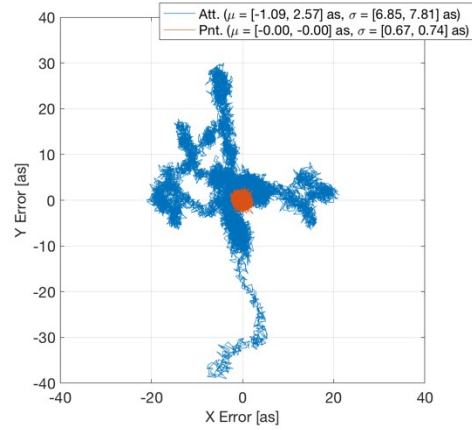


Figure 16: Attitude & Pointing Error Scatter Plot for 55 Cancri Observation.

It is also interesting to note that the attitude errors are larger than those observed in the HD 219134 observation. These errors are not initial transients that settle out over time. Figure 17 shows that these errors actually appear in the middle of the observation after a period of stable attitude control. These attitude errors vary from observation to observation and are likely due to environmental torques (mostly magnetic torque and aerodynamic drag) and are therefore very much dependent upon the orbit and attitude geometry.

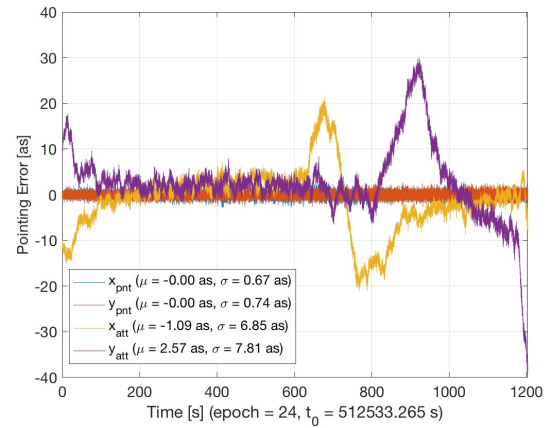


Figure 17: Attitude & Pointing Error vs. Time for 55 Cancri Observation.

Payload Pointing Performance (Alpha Centauri)

The star field around Alpha Centauri was also observed, which provides another data point showing how the performance changes with the number and brightness of the target and guide stars.

Figure 18 shows the selected target and guide stars for this observation. The target star is Alpha Centauri A (HIP 71683), which was actually merged with Alpha Centauri B and has a combined V magnitude of -0.3 . The other guide star, Beta Centauri, has a V magnitude of 0.6 . Since Alpha Centauri is so bright, the integration time of the imager actually needed to be reduced from the nominal value of 50 milliseconds to 15 milliseconds. Even with this lowered integration time, the brightest pixel on Alpha Centauri was still saturated and, for future observations, the integration time will be reduced further. While this does not seem to have a significant effect on centroiding performance, it does degrade the photometric performance.

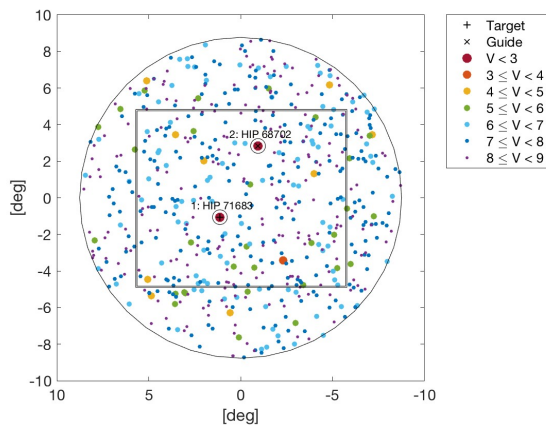


Figure 18: Selected Target and Guide Stars for Alpha Centauri Observation.

Figure 19 shows the attitude and pointing error scatter plot. Due to the brighter guide stars, even with a smaller number of total stars, the pointing stability was improved to 0.3 arcsec RMS over 15 minutes.

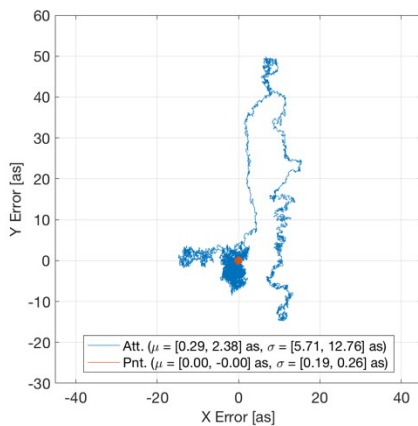


Figure 19: Attitude & Pointing Error Scatter Plot for Alpha Centauri Observation.

Similar to the 55 Cancri observation, the large attitude error transient actually occurred well into the observation, as can be seen in Figure 20. While these attitude errors seem quite large (up to 50 arcseconds), this is still very far away from the limits of the piezo stage (± 120 arcseconds).

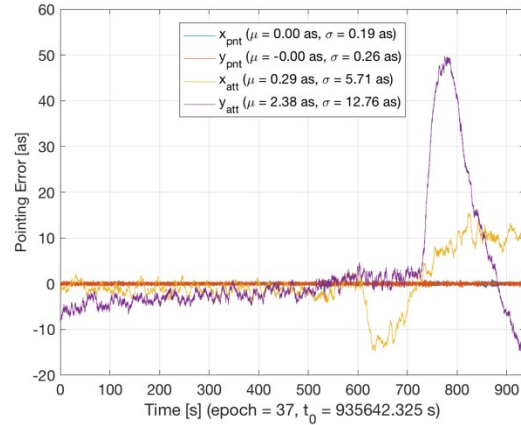


Figure 20: Attitude & Pointing Error vs. Time for Alpha Centauri Observation.

XACT-Only Pointing Performance (Alpha Centauri)

Since other missions are interested in how the XACT performs by itself, observations have been performed without the pointing control subsystem active. This means that both the piezo stage and the payload feedback to the XACT were disabled for these observations. The payload is on, centroiding the target and guide stars, and therefore measuring the pointing performance. However, only the XACT is providing the actual pointing control. In addition, the XACT gains were set to a higher, more typical bandwidth to achieve better pointing performance with the attitude control alone.

For this observation, the same Alpha Centauri star field shown in Figure 18 was being observed by the payload. Note that the star tracker and payload fields of view do not overlap since the star tracker boresight is offset by 10 degrees relative to the payload boresight.

Figure 21 and Figure 22 shows the payload cross-boresight pointing error scatter plot and pointing error versus time, respectively, for the case of XACT-only pointing control. The first thing to observe in this plot is that the amount of high-frequency noise in the pointing error is larger than that seen in the previous observations. This is due to the higher gains that were used in this observation versus the previous observations. These higher gains result in more of the star tracker noise feeding back into the control loop,

therefore increasing the high-frequency noise in the system. While the amount of high-frequency noise is increased, there are no longer any large deviations in attitude error from environmental torques, as seen in Figure 17 and Figure 20, which were eliminated by the higher bandwidth of the attitude control system.

Even though there are no large attitude deviations, there is a low-frequency bias and drift, which dominates the error in the y -axis. This is attributed to changes in alignment between the star tracker and payload. This shows that the alignment has an initial bias of 10-20 arcseconds and drifts by up to 20 arcseconds over the 20-minute observation, which is similar to what was observed in Figure 13. As noted previously, this drift is due to the geometry and materials used in the structure between the star tracker and payload and the temperatures experienced by these parts and therefore may or may not be representative of what other missions might experience.

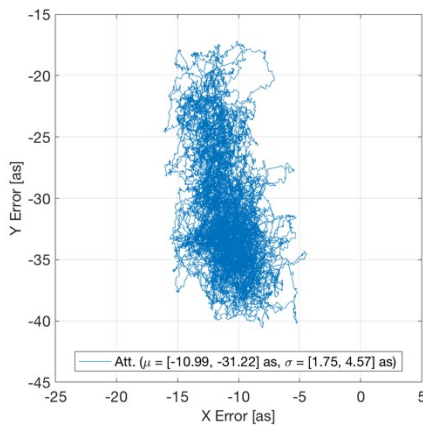


Figure 21: XACT-Only Payload Pointing Error Scatter Plot for Alpha Centauri Observation.

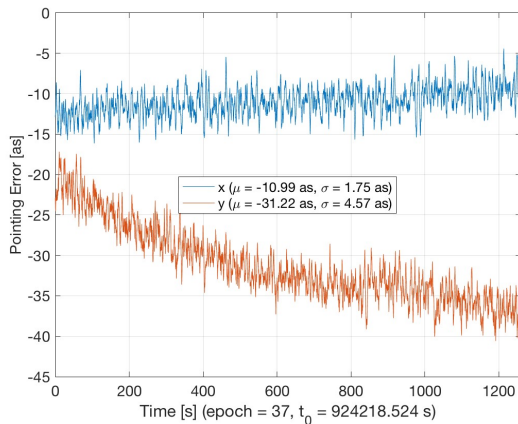


Figure 22: XACT-Only Payload Pointing Error vs. Time for Alpha Centauri Observation.

For other missions, if this low-frequency drift were removed, the pointing stability could be greatly improved. The exact improvement can be calculated by examining at the cumulative integral of the pointing error PSD, integrated from infinity to zero, shown in Figure 23. At low frequencies, this settles to a value of 2.5 arcseconds squared, which is the MSV, before jumping up to a higher value due to the bias and drift. The square root of this is 1.6 arcseconds, which is the RMS value. This says that if this low-frequency error can be removed, the pointing stability would be 1.6 arcseconds RMS over 20 minutes. One way this can be achieved is by designing the spacecraft specifically to reduce the alignment changes due to thermal effects. Another way this can be achieved is with feedback from the payload to the XACT. The payload would just need to provide updated attitude commands to the XACT to compensate for the changing alignment between the payload and star tracker.

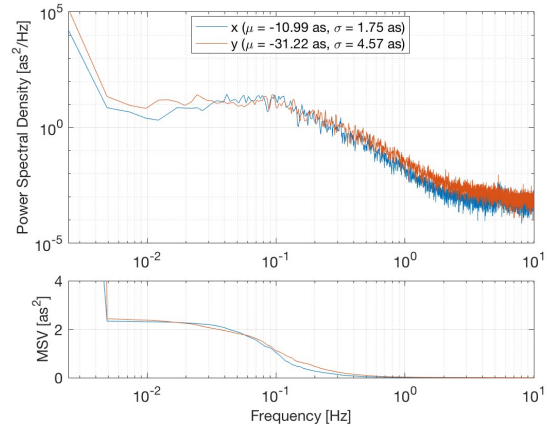


Figure 23: XACT-Only Payload Pointing Error Power Spectral Density and Mean Square Value for Alpha Centauri Observation.

Figure 24 shows the roll pointing error over time. This shows an initial bias of 130 arcseconds and a drift of 30 arcseconds over the 20 minutes, which is comparable to what was observed in Figure 12. With a low-frequency feedback from the payload to the XACT or improved star-tracker-to-payload alignment stability, the roll stability could be reduced from 9 arcseconds to 6 arcseconds RMS over 20 minutes.

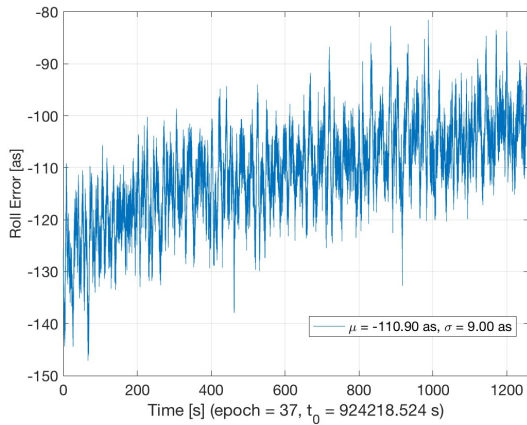


Figure 24: XACT-Only Payload Roll Error vs. Time for Alpha Centauri Observation.

Pointing Issues & Workarounds

While the attitude and pointing control subsystems on ASTERIA have performed beautifully during science observations, as seen in the previous section, there have also been a fair amount of issues that have been encountered. Some of these issues and the resulting operational workarounds will be discussed in this section.

Temporarily Bright Pixels (South Atlantic Anomaly)

Fairly early on in the mission, it was observed that the imager acted as a radiation detector. Figure 25 shows the brightest pixel value (with the column offsets subtracted) over a 42-by-42-pixel area for seven windows. It can be seen that there are a large number of temporarily bright pixels for the first 300 seconds and much less for the remainder of the observation.

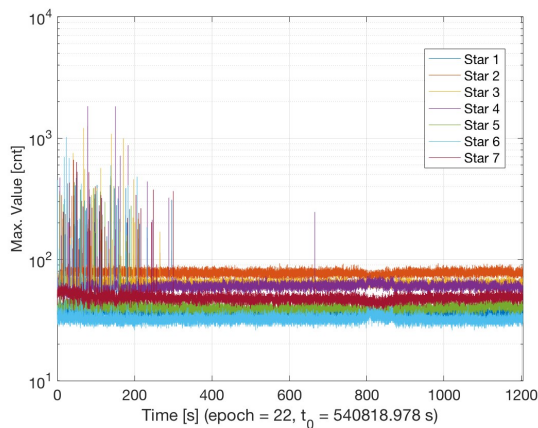


Figure 25: Maximum Pixel Value in Each Window while Exiting South Atlantic Anomaly.

It turns out that these temporarily bright pixels were observed while the spacecraft was passing through the South Atlantic Anomaly (SAA). Figure 26 shows the location of the spacecraft over Earth during this observation and it can be seen that the spacecraft was in the SAA for the first part of the observation.

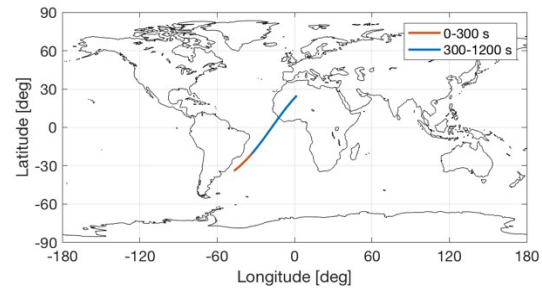


Figure 26: Spacecraft Location over Earth during Observation with Temporarily Bright Pixels.

These temporarily bright pixels occurred at a rate of approximately 1 event per second. Each time this occurred, the centroiding algorithm would think that this bright pixel was the star (since this would be brighter than the star) and would cause a small pointing error transient from the control system reacting to this change in control error. Because of this, as a part of sequence generation, the location of the spacecraft for each observation would be shown so that observations could be scheduled to avoid the SAA.

Hot Pixels

Another problem encountered with the imager is that it has a fair number of hot pixels. These are pixels with a larger-than-average dark current. Due to limited testing on the ground, it was not discovered until operations that the hot pixels measured in the full-frame mode do not seem to correlate with hot pixels that are measured in the windowed mode. In other words, hot pixels measured in a full-frame image may not show up as hot pixels in a windowed image, and vice versa. But, in a given mode, they remain in fixed locations. The resulting effect is that whenever a new star field with different window locations is observed, it is possible that new hot pixels will be uncovered. Figure 27 shows an example of a windowed image of a star with two hot pixels nearby. Note that this is an image coadded over one minute's worth of 50-millisecond exposures.

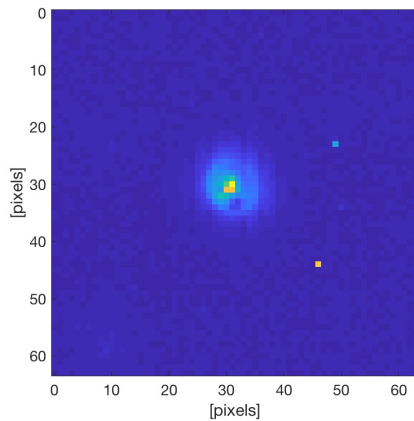


Figure 27: Example Image of a Star with Two Nearby Hot Pixels.

The brighter of the two hot pixels has a large enough dark current that it can appear brighter than the brightest pixel in the image of the star for a fraction of the images. When this occurs, the centroiding algorithm will actually set the hot pixel as the center of the region of interest over which the centroid is computed, causing the centroid to appear at a different location for one control cycle. This results in a small pointing error transient due to the control system reacting and settling to this sudden change in pointing error. Figure 28 shows the pointing error for an observation that used the guide star window shown in Figure 27. Note that this figure only shows the effect of the control system reacting to the hot pixel. The change in pointing error due to the hot pixel itself is not real and was removed in post processing the telemetry from this observation.

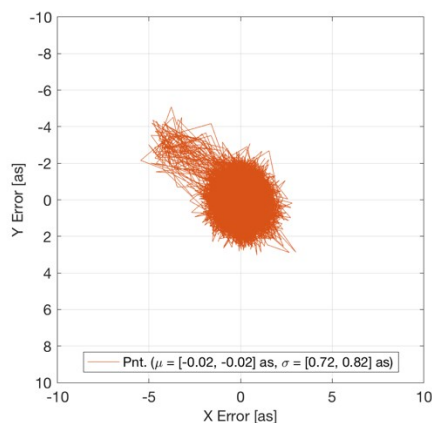


Figure 28: Effect of a Hot Pixel on Pointing Error.

For the majority of the observation, the pointing control would keep the pointing error in a circle centered around zero. However, the hot pixel is what causes the small pointing error excursion from this circle.

To fix this issue, the centroiding algorithm had to be changed to be more robust to these hot pixels. Instead of blindly taking the brightest pixel as the center of the centroiding region of interest, the brightest pixel now must also have at least one other orthogonally adjacent pixel that is brighter than a given threshold above the background. This greatly reduces the impact of hot pixels since it is unlikely for hot pixels to be orthogonally adjacent to each other and will therefore affect the centroiding algorithm with a much lower probability. Note that hot pixels that land on or very near to the guide star will still cause issues.

Before this fix was implemented, star window locations would need to be tweaked to ensure that there were no hot pixels in the windows. This was very time consuming as moving the windows could uncover further hot pixels. Another possible solution would be to create a hot pixel map for the imager in the windowed mode, which would also be very time consuming.

Reaction Wheel Speed Reversals

Another issue that affects the pointing performance is the occurrence of reaction wheel speed reversals or zero crossings. As will be discussed in the Momentum Management & Residual Dipole section on page 15, reaction wheel speed reversals are harder to avoid due to the larger reaction wheel speed range from the residual dipole. Figure 29 shows the attitude error (not pointing error) during an observation in which three separate speed reversals occurred. The attitude error due to these speed reversals produce transients on the order of 200 arcseconds and last for roughly 20 to 80 seconds. This is larger than the piezo stage range and produces motions that are faster than the piezo stage can track, therefore also negatively affect the pointing error. It can be seen that these reaction wheel speed reversals primarily affect only one axis while the other two axes remain largely unaffected. Note that the errors are reported in the payload imager frame (as opposed to the spacecraft frame shown in Figure 2) with the x - and y -axes in the horizontal and vertical directions of the imager plane and the z -axis aligned with the boresight of the payload.

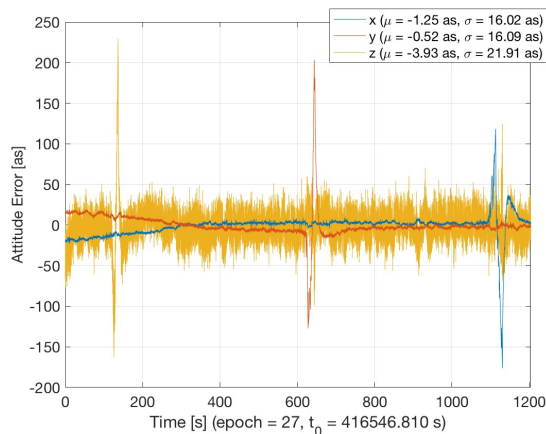


Figure 29: Attitude Errors During Reaction Wheel Speed Reversals.

These attitude error transients correlate well with reaction wheel speed reversals, as seen in Figure 30. Note that this plot exhibits artifacts that are due to poor data sampling of the XACT telemetry during an observation. The 20 Hz pointing control loop runs with the highest priority and is processor and I/O intensive. Therefore the 5 Hz task that handles the XACT commands and telemetry is not able to be serviced consistently, resulting in stale telemetry and inconsistent sampling. Nevertheless, the approximate times at which the reaction wheels cross through zero speed can be interpolated by eye. When each wheel speed crosses through zero, the resulting attitude error transient is observed on the expected axis. The reaction wheel 1/2/3 is aligned with the payload $z/x/y$ -axis, so when that wheel crosses through zero speed, it results in a $z/y/x$ -axis attitude error transient.

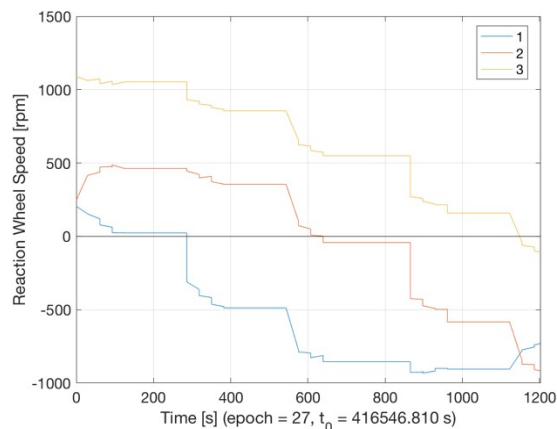


Figure 30: Reaction Wheel Speed Showing Zero Crossings.

In theory, these reaction wheel speed reversals can be avoided during observations by commanding the XACT

to have a momentum bias in the inertial frame such that the reaction wheel speeds are all, for example, 1000 rpm while in a particular inertially-fixed attitude. In practice, this can be difficult to achieve due to the large changes in reaction wheel speed that can be experienced. As seen in Figure 30, the reaction wheels varied by more than 1000 rpm over the 20-minute observation. While larger momentum biases can be commanded, this increases the chance saturating the reaction wheels, which would also cause significant pointing errors. Nevertheless, through the mitigations described in the Momentum Management & Residual Dipole section on page 15, reaction wheel speed reversals have been able to be avoided in many observations.

Deployment & Sun Acquisition

As on many spacecraft, deployment and Sun acquisition are critical events as it drives many aspects of the design of the hardware, software, and operations of the spacecraft. This was especially true for ASTERIA since (1) the spacecraft must be able to survive on its own for up to 180 days from delivery to NanoRacks, through launch, to deployment from the ISS (the batteries cannot be charged during this time), (2) the team has no control over when the spacecraft will be deployed, so ground station contact will very likely not be available and the spacecraft must be able to perform all necessary actions to survive on its own, (3) for the first 30 minutes after deployment, the spacecraft must not control its attitude or deploy the solar arrays, (4) the solar arrays must be deployed to expose any of the solar cells, (5) the spacecraft is likely not power positive while it is tumbling, and (6) ASTERIA was one of the first 6U CubeSats to be deployed, so there was no prior data on the tipoff rates of 6U CubeSats. Despite all of this, deployment and Sun acquisition went about as well as could be hoped.

Figure 31 shows the sun sensor diode counts once the flight computer and XACT were powered on 30 minutes after deployment. The initial spacecraft rates were less than 1 degree per second on all three axes. Since the spacecraft rates were low and the spacecraft was deployed during orbit day, the XACT was able to find, acquire, and settle on the Sun within 150 seconds, allowing the spacecraft to begin recharging the batteries. Around 450 seconds, the spacecraft entered orbit night and at 2650 seconds, the XACT finds the Sun again and keeps the spacecraft pointed at the Sun for the full orbit day. One interesting feature of Figure 31 is that it shows the sun sensor diode counts increase at orbit dawn and dusk. This is likely due to the illuminated Earth limb causing an increase in flux received by the diodes.

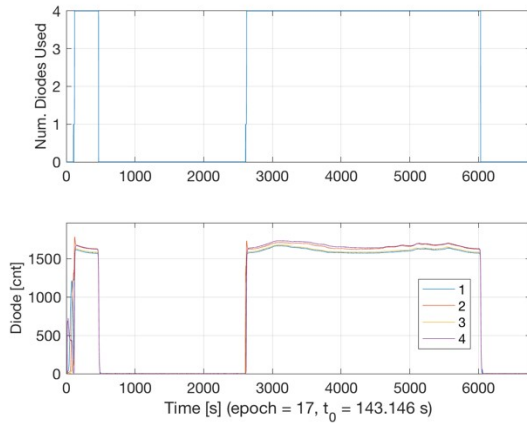


Figure 31: Sun Sensor Diode Counts after Deployment.

The autonomous capability of the XACT to quickly acquire the Sun set ASTERIA up for a good start to the mission.

Momentum Management & Residual Dipole

Another key ACS capability is the management of momentum buildup in the reaction wheels due to external environmental disturbance torques acting on the spacecraft. This was not anticipated to be a problem, until a month before spacecraft delivery. Requirements on the location of the center of mass and residual magnetic dipole moment were levied on the flight system to ensure that the aerodynamic drag and magnetic torque were low enough such that the resulting change in momentum could be controlled to a certain range. Due to limited time and money, the residual dipole was never estimated based on the location of various components and materials within the spacecraft. Instead, the residual dipole was to be measured once the spacecraft was complete and, if necessary, add trim magnets to reduce the residual dipole. Measurements of the center of mass (shown in Table 2) came in within the requirement, however the residual dipole was well outside of the requirement.

The residual magnetic dipole moment of the spacecraft was estimated from measurements of the magnetic field at various points around the spacecraft. Figure 32 shows a picture of one magnetic field measurement with the spacecraft in the background and the magnetometer at a known distance away from the spacecraft in the foreground. Measurements were taken in an anechoic chamber to reduce the effect of external magnetic sources and the magnetic field due to sources other than the spacecraft were subtracted from the measurements.

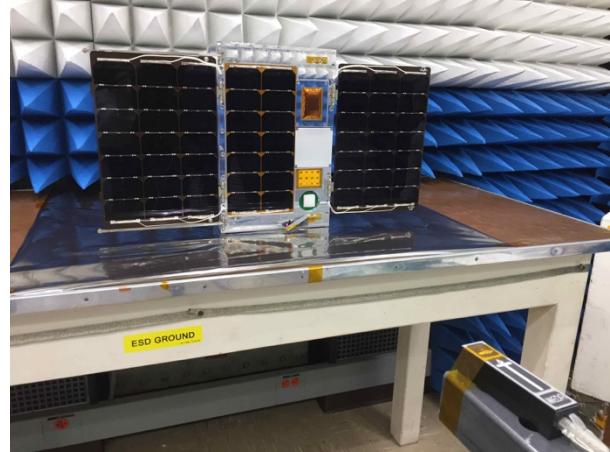


Figure 32: Magnetic Field Measurement of ASTERIA.

Measurements of the magnetic field were taken at various distances for all six sides of the spacecraft. A dipole model was then fit to these measurements using a nonlinear least-squares optimization. Figure 33 shows the magnitude and direction of the measured and modeled magnetic field at the various measurement locations around the spacecraft. Visually, the model matches the measurements fairly well and shows a significant dipole in the $-z$ -direction. The estimated residual magnetic dipole moment was -0.004 Am^2 (x -axis), 0.005 Am^2 (y -axis), and -0.168 Am^2 (z -axis). This is a very large residual dipole, especially considering that the XACT torque rods for ASTERIA produce a smaller dipole of 0.125 Am^2 . At this point, there was not enough programmatic margin to figure out what was causing this large residual dipole or attempt to reduce it either with a bulk tape eraser or using trim magnets. Instead, the spacecraft was delivered, launched, and deployed with this large residual dipole.

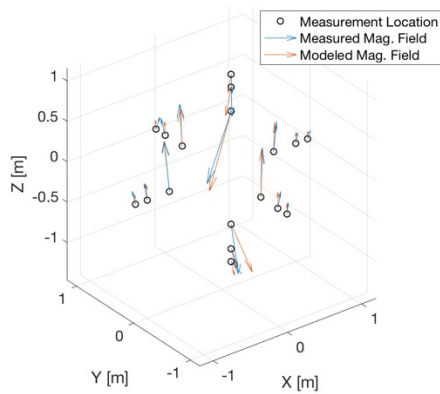


Figure 33: Measured and Modeled Magnetic Field at Various Points Relative to ASTERIA.

This residual dipole has a significant effect on the momentum management. Since the residual dipole is roughly aligned with the $-z$ -axis and the solar array normal are aligned with the $+z$ -axis, there is no choice in how to orient the residual dipole vector when the XACT is pointing the solar arrays to the Sun. Interestingly, when the orbit beta angle is close to zero, which occurs roughly once a month, the torque rods have a more difficult time dumping the momentum due to the residual dipole. XACT telemetry from this period of time will be shown to demonstrate some of the momentum management challenges due to the residual dipole.

Figure 34 shows a plot of the XACT's estimate of the momentum norm of the spacecraft, which includes the reaction wheels and spacecraft rate. It is important to note that no momentum bias was commanded, so the momentum seen in the plot is purely from buildup due to the external torques. The plot shows that there were instances where the wheels hit saturation over a period of 4 orbits. The plot exhibits some artifacts due to quantization of telemetry and some high-frequency motion due to a mismatch between the inertia initially programmed in the XACT versus the actual flight inertia shown in Table 2. Since the mission did not require a very accurate inertia knowledge, resources were not spent to update the inertia in the XACT.

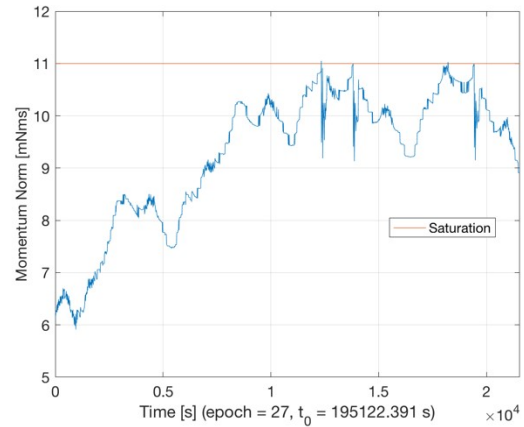


Figure 34: Momentum Norm Showing a Large Momentum Buildup.

A plot of the sun sensor diodes in Figure 35 show that the spacecraft does indeed lose attitude control during three instances of hitting saturation. The spacecraft points off the Sun for about 4 minutes during each of these instances.

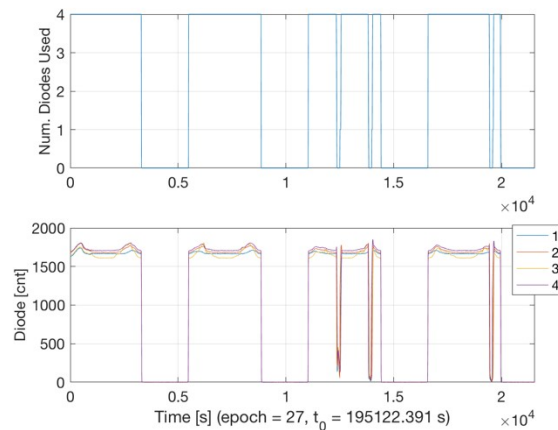


Figure 35: Sun Sensor Diode Counts Showing Short Periods of Attitude Control Loss.

Because the spacecraft is pointing the residual dipole vector away from the Sun for extended periods of time, for certain orbit geometries momentum is allowed to build up, causing these instances of temporary attitude control loss. This was verified in simulation by seeing the effect of the increased residual dipole on momentum buildup for the actual orbit and attitude trajectories experienced by the spacecraft. In fact, simulations show that the residual dipole seems to be approximately 50% larger than what was measured on the ground. It is unclear how this could be the case. Nevertheless, one mitigation for this effect is to spin the spacecraft during orbit night. This causes the residual

dipole vector to be spun around, which keeps the momentum from building up during orbit night.

While it may sound strange, the temporary loss of attitude control due to momentum buildup while pointed at the Sun is actually not that big of a problem. When these instances occur, the spacecraft is mainly just charging its batteries and it still has enough time to recharge the batteries even with a temporary loss of attitude control. The bigger problem posed by the residual dipole is that it undermined the planned approach to avoid wheel speed reversals during science observations. Because of the large residual dipole, the reaction wheel speed range is larger than originally anticipated. This means that the wheels must be biased to higher wheel speeds during an observation to avoid speed reversals. However, if the wheels are biased too high, there is an increased risk of approaching saturation. To handle this issue, a couple tactics have been deployed. First, the science observation sequence generation tool includes a simulation that predicts the reaction wheel speeds over time. This allows one to see how close the wheel speeds are to crossing through zero or approaching saturation and adjust the momentum bias accordingly. And second, the science observations can be modified to have a different roll angle about the payload boresight. Since the residual dipole vector is roughly aligned with the $-z$ -axis and the payload boresight is aligned with the $+x$ -axis, how momentum changes over an orbit can be modified by changing the roll angle. Even with these mitigations, reaction wheel zero crossings can still occur. The Reaction Wheel Speed Reversals section on page 13 describe the effect on pointing if a speed reversal occurs.

XACT Anomalies

Over the course of the mission, the XACT has experienced several anomalies. Table 3 shows a list of all of the XACT anomalies that have occurred to date (six months into the mission as of this writing). While some of these anomalies resulted in a loss of attitude control, the spacecraft operators or on-board spacecraft fault protection caught the anomaly, power cycled the XACT, and recovered the spacecraft. Power cycling the XACT has been shown to fix all issues involving the XACT so far. It is interesting to note that all of the anomalies have occurred in the first three months of the mission, serving as “fun” opportunities to train the operations team. Also, there is no strong correlation of these events with either being in the SAA or with space weather events. In communication with BCT, it is clear that ASTERIA has experienced the majority of on-orbit XACT anomalies compared to other missions that have flown the XACT.

Table 3: List of XACT Anomalies.

UTC	Event
2017/11/20 12:25:01	Spacecraft deployment
2017/11/25 03:42:49	XACT anomaly 1
2017/12/05 20:21:03	Commanded XACT power cycle
2017/12/20 20:51:50	XACT anomaly 2a
2017/12/21 22:14:18	Commanded XACT power cycle
2017/12/23 23:58:18	XACT anomaly 2b
2017/12/24 13:06:53	Commanded XACT power cycle
2018/01/24 01:34:49	XACT anomaly 3
2018/01/24 03:28:14	Commanded XACT power cycle
2018/02/20 23:38:58	XACT anomaly 2c
2018/02/20 23:58:05	Commanded XACT power cycle

XACT Anomaly 1

The first anomaly that was encountered occurred only five days into the mission. The spacecraft did not appear to be in any danger and the XACT was able to continue pointing the spacecraft to the Sun during orbit day. So, it was decided that checkouts of other subsystems should continue before the XACT power cycle was commanded as a hedge against the very low probability that the spacecraft would be lost after an XACT power cycle.

Finally, after 12 days since the anomaly onset, the XACT was power cycled. This means the power to the XACT was actually disabled, then reenabled. Afterward, the XACT performed nominally.

XACT Anomaly 2

The next type of XACT anomaly actually occurred three times: twice in the days leading up to Christmas, then once again a couple months later. This was a potentially mission-threatening anomaly. Luckily, the spacecraft was at a high beta angle, meaning the initial temperatures and battery voltage were high enough that the operations team could identify and recover this anomaly without relying on on-board fault protection. The operations team noticed this issue on the first communication pass and power cycled the XACT on the next communication pass, after which the XACT performed nominally.

When this anomaly occurred three days later, the operations team was ready for this fault and the XACT was power cycled on the same communication pass where the abnormal behavior was observed. Again, the power cycle fixed the issue.

The ASTERIA flight software was updated to include a fault monitor that would power cycle the XACT if this anomaly occurred again. When the anomaly occurred

for the third time, this new fault monitor was tripped, the XACT was power cycled autonomously, and XACT returned to nominal behavior, greatly increasing confidence in being able to handle future instances of this anomaly. Since ASTERIA, XACT software has been upgraded to autonomously identify and recover this type of anomaly.

XACT Anomaly 3

The last type of anomaly that was observed occurred only once. This was another potentially mission-threatening anomaly as it resulted in the spacecraft tumbling, causing temperatures and battery voltages to drop. The team was experiencing unrelated difficulties contacting the spacecraft at the time, so the on-board fault protection was the only safety net. The battery undervoltage fault monitor was tripped, resulting in the spacecraft resetting, which included power cycling the XACT. Right after the XACT powered back on, attitude control was reestablished and the spacecraft was pointed at the Sun within seconds. As a result of this anomaly, ASTERIA's fault protection was updated to include another monitor for this fault, but this anomaly has not reoccurred.

CONCLUSION

The first few months of operations of ASTERIA have been fun, interesting, and stressful. The XACT anomalies that were experienced were a great way to train the operations team as many involved were early-career hires and also really put the ASTERIA fault protection and flight software through its paces. Hopefully the experience of ASTERIA can help improve the robustness of other missions.

Despite the challenges associated with the residual dipole, momentum management, reaction wheel speed reversals, and temporarily bright and hot pixels, the XACT and PCS were able to provide the best pointing performance on a CubeSat or spacecraft of similar size to date. The XACT and PCS combined were able to achieve a pointing stability of 0.5 arcsecond RMS over 20 minutes and 1 milliarcsecond RMS from observation to observation. Note that this number can vary, depending on the number and brightness of the guide stars being observed. It is also interesting to note that while there was an accepted risk that ASTERIA might experience thermal snap events similar to what Hubble experienced⁹ during orbit night/day transitions, this effect has not been observed in telemetry so far.

The pointing performance of the XACT alone was also measured with the ASTERIA payload. One observation showed a pointing stability of 1.8 to 4.6 arcseconds RMS over 20 minutes, which is quite good. In fact, this performance could have met ASTERIA's stability

requirement of 5 arcseconds RMS over 20 minutes (though likely not the repeatability requirement). In addition, most of this error is dominated by the payload-to-star-tracker alignment stability, which shows up in the data as a low-frequency wandering. If payload feedback to the XACT were employed or if the spacecraft were specifically designed to reduce the changes in alignment due to thermomechanical distortion, this error could have easily been reduced to 1.6 arcseconds RMS over 20 minutes for both axes.

ASTERIA is currently operating on an extended mission, which will continue as long as funding allows. While this paper focuses on early mission ACS and PCS results, future publications will describe the details of the hardware, algorithms, modeling, simulation, and analysis.

ACKNOWLEDGMENTS

The work was carried out at the Jet Propulsion Laboratory, California Institute of Technology, under a contract with the National Aeronautics and Space Administration. © 2018 California Institute of Technology. Government sponsorship acknowledged. Reference herein to any specific commercial product, process, or service by trade name, trademark, manufacturer, or otherwise, does not constitute or imply its endorsement by the United States Government or the Jet Propulsion Laboratory, California Institute of Technology.

The following people are acknowledged for their work that made this paper possible:

Matt Baumgart (BCT), Bryan Rogler (BCT), and Matt Carton (BCT) for their extensive knowledge and support of the XACT.

Sara Seager (MIT) and Brice-Olivier Demory (University of Bern) for providing the science case for ASTERIA and supporting the mission. Mary Knapp (MIT) for the above and for planning the science observations.

The JPL Phaeton program for funding this mission. The JPL line, program, project, mission managers, and ASTERIA mentors for their support. Paul Brugarolas for providing guidance and control mentorship throughout ASTERIA mission. Matthew W. Smith, Lori Moore, Janan Ferdosi, Harrison Herzog, and Shannon Zareh for designing and integrating the payload. Chris Shelton and Jason Luu for designing and building the piezo stage electronics. Thomas Werne, David Kessler, and Carl Felten for delivering the firmware and software to interface with the payload. Len Day, Brian Campuzano, Rob Bocchino, Kevin

Dinkel, and Jim Hofman for coding the flight software. Amanda Donner for fault protection, quality assurance, and mission assurance. Cody Colley and his team for integrating and testing the spacecraft. Esha Murty and Keith Fields for performing the mass properties measurements. Kevin Pham, Maria de Soria-Santacruz Pich, and Pablo Narvaez for testing the residual magnetic dipole moment. Brian Okimoto for assistance testing the XACT. The ASTERIA operations team, including those at Morehead State University, for successfully flying the mission.

REFERENCES

1. Smith, M. W., Seager, S., Pong, C. M., Villaseñor, J. S., Ricker, G. R., Miller, D. W., Knapp, M. E., Farmer, G. T., and Jensen-Clem, R., "ExoplanetSat: Detecting transiting exoplanets using a low-cost CubeSat platform," *Proceedings of SPIE*, Vol. 7731 Space Telescopes and Instrumentation 2010: Optical, Infrared, and Millimeter Wave, San Diego, CA, June–July 2010, p. 773127.
2. Pong, C. M., Lim, S., Smith, M. W., Miller, D. W., Villaseñor, J. S., and Seager, S., "Achieving high-precision pointing on ExoplanetSat: Initial feasibility analysis," *Proceedings of SPIE*, Vol. 7731 Space Telescopes and Instrumentation 2010: Optical, Infrared, and Millimeter Wave, San Diego, CA, June–July 2010, p. 77311V.
3. Pong, C. M., Smith, M. W., Knutson, M. W., Lim, S., Miller, D. W., Seager, S., Villaseñor, J. S., and Murphy, S. D., "One-Arcsecond Line-of-Sight Pointing Control on ExoplanetSat," *Guidance and Control 2011*, Vol. 141 of Advances in the Astronautical Sciences, AAS, Univelt, Inc., Breckenridge, CO, February 2011, pp. 147–166.
4. Smith, M. W., Seager, S., Pong, C. M., Knutson, M. W., Miller, D. W., Henderson, T. C., Lim, S., Brady, T. M., Matraga, M. J., and Murphy, S. D., "The ExoplanetSat Mission to Detect Transiting Exoplanets with a CubeSat Space Telescope," *Small Satellite Conference*, AIAA/USU, Utah State University Research Foundation, Logan, UT, August 2011, pp. 1–9.
5. Pong, C. M., Knutson, M. W., Miller, D. W., Seager, S., Lim, S., Henderson, T. C., and Murphy, S. D., "High-Precision Pointing and Attitude Determination and Control on ExoplanetSat," *AIAA Guidance, Navigation, and Control Conference*, Minneapolis, MN, August 2012, pp. 1–24.
6. Knapp, M., Smith, M., Pong, C., Nash, J., and Seager, S., "ExoplanetSat: High Precision Photometry for Exoplanet Transit Detections in a 3U CubeSat," *63rd International Astronautical Congress*, IAF, Naples, Italy, October 2012, pp. 1–12.
7. Pong, C. M., Seager, S., and Miller, D. W., "Three-Degree-of-Freedom Testing of Attitude Determination and Control Algorithms on ExoplanetSat," *Guidance and Control 2014*, Vol. 151 of Advances in the Astronautical Sciences, AAS, Univelt, Inc., Breckenridge, CO, February 2014, pp. 285–307.
8. Pong, C. M., *High-Precision Pointing and Attitude Estimation and Control Algorithms for Hardware-Constrained Spacecraft*, Doctor of Science thesis, Massachusetts Institute of Technology, Cambridge, MA, May 2014.
9. Nurre, G. S., Sharkey, J. P., Nelson, J. D. and Bradley, A. J. (1995) "Preservicing Mission, On-Orbit Modifications to Hubble Space Telescope Pointing Control System," *Journal of Guidance, Control, and Dynamics*, Vol. 18, No. 2, March–April 1995, pp. 222–229.
10. "User Documentation for Cycle 1: JWST Observatory," JWST Cycle 1 Documentation for Telescope and Spacecraft, <https://jwst-docs.stsci.edu>, 12 February 2018.
11. Blackmore, L., Murray, E., Scharf, D. P., Aung, M., Bayard, D., Brugarolas, P., Hadaegh, F., Kang, B., Lee, A., Milman, M., and Sirlin, S., "Instrument Pointing Capabilities: Past, Present and Future," *Guidance and Control 2011*, Vol. 141 of Advances in the Astronautical Sciences, AAS, Univelt, Inc., Breckenridge, CO, February 2011, pp. 675–692.
12. Liu, K.-C., Blaurock, C. A., Bourkland, K. L., Morgenstern, W. M., and Maghami, P. G., "Solar Dynamics Observatory On-orbit Jitter Testing, Analysis, and Mitigation Plans," *AIAA Guidance, Navigation, and Control Conference*, Portland, OR, August 2011, pp. 1–28.
13. Marcos-Arenal, P., et al., "The PLATO Simulator: modelling of high-precision high-cadence space-based imaging," *Astronomy & Astrophysics*, Vol. 566, No. A92, June 2014, pp. 1–12.
14. Schira, C. N. and Putnam, D. S., "Kepler ADCS Overview and Early Mission Experiences," *Guidance and Control 2010*, Vol. 137 of Advances in the Astronautical Sciences, AAS,

- Univelt, Inc., Breckenridge, CO, February 2010, pp. 761–774.
15. Bayard, D. S., “Advances in Precision Pointing Control for the NASA Spitzer Space Telescope,” *Guidance and Control 2004*, Vol. 118 of Advances in the Astronautical Sciences, AAS, Univelt, Inc., Breckenridge, CO, February 2004, pp. 527–546.
 16. Auvergne, M., et al., “The CoRoT satellite in flight: description and performance,” *Astronomy & Astrophysics*, Vol. 506, No. 1, October 2009, pp. 411–424.
 17. Hynes, S., “Transiting Exoplanet Survey Satellite (TESS) Mission: Searching for Exoplanets on an Explorer Budget,” *Systems Engineering Seminar*, Applied Engineering Technology Directorate at NASA Goddard Space Flight Center, Greenbelt, MD, September 2017.
 18. Fortier, A., “CHEOPS Instrument and Performance,” *III CHEOPS Science Workshop*, Madrid, Spain, July 2015.
 19. Grocott, S. C. O., Zee, R. E., Matthews, J., “The MOST Microsatellite Mission: One Year In Orbit,” *18th Annual AIAA/USU Conference on Small Satellites*, Logan, UT, August 2004, pp. 1–12.
 20. Sarda, K., Grant, C., Chaumont, M., Choi, S. Y., Johnston-Lemke, B., and Zee, R., “On-Orbit Performance of the Bright Target Explorer (BRITE) Nanosatellite Astronomy Constellation,” *28th Annual AIAA/USU Conference on Small Satellites*, Logan, UT, August 2014, pp. 1–18.
 21. Mason, J. P., et al., “MinXSS-1 CubeSat On-Orbit Pointing and Power Performance: The First Flight of the Blue Canyon Technologies XACT 3-axis Attitude Determination and Control System,” *Journal of Small Satellites*, Vol. 6, No. 3, December 2017, pp. 651–662.
 22. Janson S., et al., “The NASA Optical Communication and Sensor Demonstration Program: Initial Flight Results,” *30th Annual AIAA/USU Conference on Small Satellites*, Logan, UT, August 2016, pp. 1–8.
 23. Smith, M. W., et al., “On-Orbit Results and Lessons Learned from the ASTERIA Space Telescope Mission,” *32nd Annual AIAA/USU Conference on Small Satellites*, Logan, UT, August 2018.
 24. High Energy Astrophysics Science Archive Research Center, “HIPPARCOS - Hipparcos Main Catalog,” <http://heasarc.gsfc.nasa.gov/W3Browse/all/hipparcos.html>.
 25. Shields, J., Pong, C., Lo, K., Jones, L., Mohan, S., Marom, C., McKinley, I., Wilson, W., Andrade, L., “Characterization of CubeSat Reaction Wheel Assemblies,” *Journal of Small Satellites*, Vol. 6, No. 1, May 2017, pp. 565–580.